A Master-Slave Model Predictive Control Approach for Microgrids

Fernanda Carnielutti, *Member, IEEE*, Mokhtar Aly, *Senior Member, IEEE*, Margarita Norambuena, *Senior Member, IEEE*, Jiefeng Hu, *Senior Member, IEEE*, Josep Guerrero, *Fellow, IEEE*, and José Rodriguez, *Life Fellow, IEEE*

***Abstract*—This article proposes a master-slave finite control set model predictive control (FCS-MPC) for microgrids. To demonstrate it, a microgrid is considered, composed of a master neutral-point clamped (NPC) inverter with a battery energy storage system (BESS) and output *LC* filter; two slave NPC inverters with photovoltaic (PV) panels and output *LCL* filters; RL and nonlinear loads. Two modes of operation are proposed for the primary control of the microgrid. In the first, the microgrid is connected to the main grid, and the master and slaves are grid-following inverters. In the second, the microgrid is islanded, and the master is a grid-forming inverter, while the slaves remain as grid-following inverters. To validate the performance of the proposed master-slave FCS-MPC, hardware-in-the-loop (HIL) results are presented for different operational conditions of the microgrid, including grid connection, transition to islanded mode, and load variations. The results demonstrate the good performance of the proposed master-slave FCS-MPC, such as fast dynamic response, multivariable control, and robustness to parametric uncertainties and variations.**

***Index Terms*—Grid-following inverters, grid-forming inverters, master-slave control, microgrids, model predictive control (MPC).**

Received 19 April 2024; revised 8 July 2024 and 15 August 2024; accepted 12 September 2024. Date of publication 19 September 2024; date of current version 12 December 2024. This work was supported in part by INCT-GD through projects under Grant CNPq 405054/2022-0, Grant CAPES 23038.000776/2017-54, and Grant FAPERGS 17/2551-0000517-1, in part by ANID under Project 1210208, Project 1221293, and Project FB0008, in part by the Advanced Center for Electrical and Electronics Engineering under Project FONDECYT 1230250, in part by FONDECYT Iniciacion under Grant 11230430, in part by SERC-Chile under Grant ANID/FONDAP/1523A0006, and in part by Australian Research Council under Grant FT240100673. Recommended for publication by Associate Editor Li (SSGAE_M) Peng. *(Corresponding author: Fernanda Carnielutti.)*

Fernanda Carnielutti is with the Campus Santa Maria and Power Electronics and Control Research Group (GEPOC), UFSM, Federal University of Santa Maria, Santa Maria 97105-900, Brazil (e-mail: fernanda.carnielutti@ufsm.br).

Mokhtar Aly and José Rodriguez are with the Department of Engineering Sciences, Universidad San Sebastian, Santiago 30332, Chile (e-mail: mokhtar.aly@uss.cl; josep.m.guerrero@upc.edu).

Margarita Norambuena is with the Department of Electrical Engineering, Universidad Tecnica Federico Santa Maria, Valparaiso 30332, Chile (e-mail: margarita.norambuena@usm.cl).

Jiefeng Hu is with the Centre for New Energy Transition Research, Federation University Australia, Mount Helen, VIC 3353, Australia (e-mail: j.hu@federation.edu.au).

Josep Guerrero is with the Center for Research on Microgrids, Department of Electronic Engineering, Technical University of Catalonia, 08019 Barcelona, Spain, also with the ICREA, 08010 Barcelona, Spain, and also with the CROM, AAU Energy, Aalborg University, 9220 Aalborg East, Denmark (e-mail: joz@energy.aau.dk).

Color versions of one or more figures in this article are available at https://doi.org/10.1109/TPEL.2024.3464105.

Digital Object Identifier 10.1109/TPEL.2024.3464105

I. Introduction

MICROGRIDS can operate connected to the main grid or islanded and are comprised of distributed generation units such as wind and photovoltaic (PV), energy storage systems (ESSs), diesel gensets, power electronics, distribution lines, loads, relays, and communication systems [1]. The microgrid control is usually divided into four levels [1], [2], [3], i.e., hierarchical control. The zero layer acts at the inverter-level for current and voltage control, virtual impedance, etc. The primary control acts in a time scale of milliseconds to seconds, performing power sharing for parallel inverters. Secondary control works in a time scale of seconds to minutes, regulating voltage and frequency deviations. Tertiary control is responsible for the interaction of the microgrid with the main grid at time scales from minutes to hours, including power flow regulation, market-driven optimal dispatch, etc.

For the primary control of microgrids, usually multiloop cascaded linear controllers are used, such as centralized or distributed control, circular chain control, average load sharing, master-slave, and droop [4], [5]. Specifically regarding master-slave, various methods were presented. Buduma et al. [6] proposed a robust control using nested linear quadratic regulators and mixed H_2/H_∞ optimal control. A linear controller with cooperative load sharing was presented in [7] for multiple master-slave microgrids. Miller et al. [8] presented a master-slave that eliminates explicit communications. Master-slave methods were presented using neural networks (NNs), such as self-constructing fuzzy NNs (SFNN) [9], data-driven three-layer NN [10], etc. Although these methods are well known and widely used, they have some disadvantages, such as inherently slow dynamic responses and difficulties in implementing multiobjective control [1]. They can also suffer from complex tuning procedures, large amounts of data for the tuning process, unstable responses to transient events, etc.

On the other hand, model predictive control (MPC) is increasingly used in microgrids [1], [2], [3], [11]. The finite control set MPC (FCS-MPC) uses the discrete-time system model to predict its future states [12], [13], [14]. At each sample k, a cost function with multiple control objectives is calculated for all systems inputs, and the one that minimizes it is selected. Therefore, FCS-MPC can directly consider system nonlinearities and operational constraints, resulting in faster dynamic responses when compared to linear controllers [11]. It can be

used in the zero and primary control layers of microgrids for current and power control, capacitor voltage control for multilevel inverters, etc. [15], [16], [17], [18], [19], [20]. It can be used in grid-forming inverters, having several advantages over conventional methods. Dragičević [21] presented an FCS-MPC for the primary control of islanded grid-forming inverters, that was extended in [22] to include secondary control. A simplified FCS-MPC was presented in [23], and a dual-loop controller based on cascaded proportional-integral and MPC was shown in [24]. Cifuentes [25] presented a model-free MPC to compensate parameter variations. An MPC with current constraints and lookup tables was provided in [26]. A modulated MPC was presented in [27], using an offline lookup table for parameter uncertainty. For secondary and tertiary control, MPC can be used for centralized [28] and distributed [29], [30] control, for frequency restoration [31], and for optimal microgrid operation [32], [33], [34], [35]. These papers demonstrated that MPC can be a flexible solution for multiobjective control of microgrids, avoiding the problems inherent to classical cascaded control structures. However, none have discussed the FCS-MPC for the master-slave operation of microgrids. Recent research efforts are directed toward demonstrating the applicability and superiority of FCS-MPC in microgrid systems, which is the topic of the current article.

In this context, this article proposes a master-slave FCS-MPC for the zero and primary control layers of microgrids, being an extension of [36]. The master is a neutral-point-clamped (NPC) inverter with a battery energy storage system (BESS) and *LC* filter. The slaves are two NPC inverters with PV panels and *LCL* filters. Two modes of operation are proposed for the primary control. In the first, the microgrid is connected to the grid, and the master and slaves are grid-following inverters. In the second, the microgrid is islanded, and the master operates as a grid-forming inverter. The microgrid is also composed of linear and nonlinear loads. The advantages of the proposed master-slave FCS-MPC over traditional linear controllers are fast dynamic response, multiobjective control, robustness against parametric uncertainties/variations, and unmodeled dynamics. The main contributions of this article are as follows.

1) While most MPC methods presented in the literature focus on a single inverter (either grid-connected or islanded), the proposed master-slave FCS-MPC coordinates multiple inverters in microgrid applications.
2) The proposed master-slave FCS-MPC controls multiple inverters in the microgrid in grid-connected and islanded modes. The inverters can be grid-forming and/or grid-following, with the same or different parameters, power ratings, output filters, etc.
3) The proposed master-slave FCS-MPC focuses on the zero and primary control layers of the microgrid.
4) For the primary control, two methods are described to generate the references for the inner FCS-MPCs of the master and slave inverters, depending on whether the microgrid is in grid-connected or islanded mode.
5) It is important to note that, up to date, there has been no research incorporating master-slave primary control together with the zero layer MPC to achieve improved microgrid performance.
6) This article is the first step toward the implementation of the master-slave FCS-MPC together with secondary and tertiary control layers in future works.

The rest of this article is organized as follows. Section II describes the Master-Slave FCS-MPC for the zero control layer. Section III presents the primary control of the microgrid. Section IV brings hardware-in-the-loop (HIL) case studies for different operational conditions. Finally, Section V concludes this article.

II. Proposed Master-Slave Finite Control Set Model Predictive Control

To present the proposed Master-Slave FCS-MPC, let us consider the microgrid of Fig. 1. The zero layer of the Master-Slave FCS-MPC corresponds to the inner FCS-MPC control loops of the NPC inverters. A higher layer is responsible for the primary control of the microgrid when grid-connected or islanded and is the main contribution of this article.

A. Master Inverter

The Master is an NPC inverter with a BESS and LC filter that is a grid-following inverter when grid-connected and a grid-forming inverter when islanded. It controls the voltages of the LC filter capacitors and the inverter-side currents to control the power injected into the grid in grid-connected mode and balances the voltages of dc bus capacitors. The discrete-time equations of the inverter-side currents and capacitor voltages of the Master in $\alpha\beta$ coordinates are

$$\begin{bmatrix} i_{m\alpha}(k+1) \\ i_{m\beta}(k+1) \end{bmatrix} = \left(1 - \frac{RT_s}{L_m}\right) \begin{bmatrix} 1 & 0 \\ 0 & 1 \end{bmatrix} \begin{bmatrix} i_{m\alpha}(k) \\ i_{m\beta}(k) \end{bmatrix} + \frac{T_s}{L_m} \begin{bmatrix} 1 & 0 \\ 0 & 1 \end{bmatrix} \begin{bmatrix} u_{m\alpha}(k) \\ u_{m\beta}(k) \end{bmatrix} - \frac{T_s}{L_m} \begin{bmatrix} 1 & 0 \\ 0 & 1 \end{bmatrix} \begin{bmatrix} v_{m\alpha}(k) \\ v_{m\beta}(k) \end{bmatrix} \tag{1}$$

$$\begin{bmatrix} v_{m\alpha}(k+2) \\ v_{m\beta}(k+2) \end{bmatrix} = \begin{bmatrix} v_{m\alpha}(k+1) \\ v_{m\beta}(k+1) \end{bmatrix} + \frac{T_s}{C_m} \begin{bmatrix} 1 & 0 \\ 0 & 1 \end{bmatrix} \begin{bmatrix} i_{m\alpha}(k+1) \\ i_{m\beta}(k+1) \end{bmatrix} - \frac{T_s}{C_m} \begin{bmatrix} 1 & 0 \\ 0 & 1 \end{bmatrix} \begin{bmatrix} i_{mo\alpha}(k+1) \\ i_{mo\beta}(k+1) \end{bmatrix} \tag{2}$$

or, in compact form

$$\mathbf{i}_{m\alpha\beta}(k+1) = \mathbf{A}_i \mathbf{i}_{m\alpha\beta}(k) + \mathbf{B}_i \mathbf{u}_{m\alpha\beta}(k) - \mathbf{F}_i \mathbf{v}_{m\alpha\beta}(k) \tag{3}$$

$$\mathbf{v}_{m\alpha\beta}(k+2) = \mathbf{v}_{m\alpha\beta}(k+1) + \mathbf{B}_c \mathbf{i}_{m\alpha\beta}(k+1) - \mathbf{F}_c \mathbf{i}_{mo\alpha\beta}(k+1) \tag{4}$$

where $\mathbf{i}_{m\alpha\beta}$ and $\mathbf{i}_{mo\alpha\beta}$ are the master inverter-side and output currents, $\mathbf{u}_{m\alpha\beta}$ are the inverter output voltages, $\mathbf{v}_{m\alpha\beta}$ are the filter capacitor voltages, T_s is the sampling period and L_m, C_m, and R are the filter parameters. The output currents $\mathbf{i}_{mo\alpha\beta}$ are measured after the filter and considered as disturbances. The

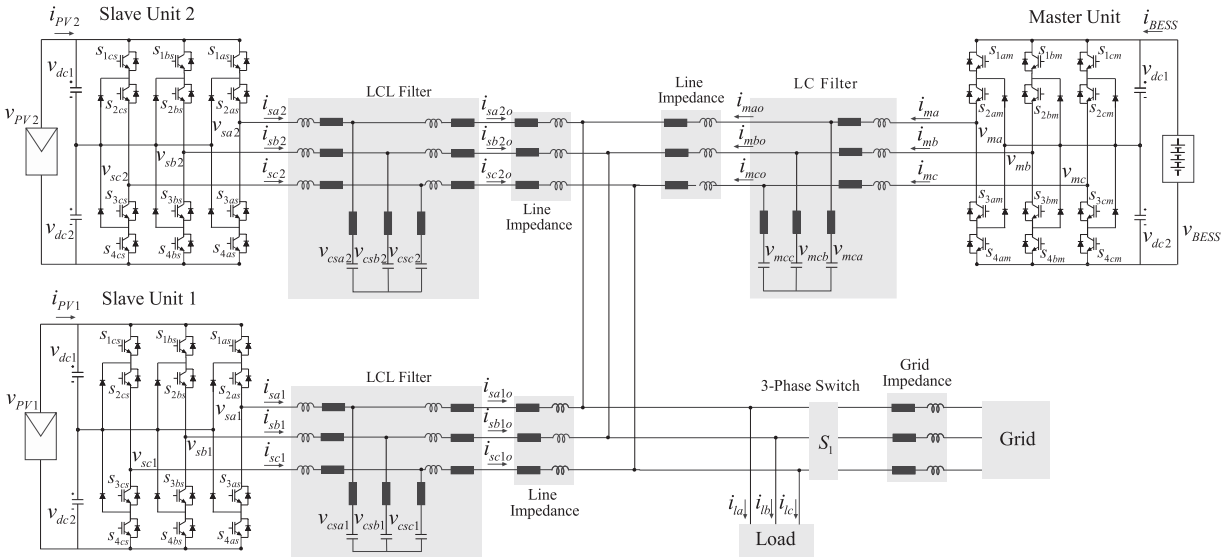

Fig. 1. Schematic of the microgrid considered as an example for the description of the proposed master-slave FCS-MPC.

models (3)–(4) were obtained by discretizing the continuous-time system with the forward Euler discretization method.

The voltages of the dc bus capacitors must also be controlled. The currents that flow through the upper and lower capacitors, respectively, i_{mdc1} and i_{mdc2}, are

$$i_{mdc1} = i_B - S_{1am}(k)i_{ma} - S_{1bm}(k)i_{mb} - S_{1cm}(k)i_{mc} \tag{5}$$

$$i_{mdc2} = i_B + S_{4am}(k)i_{ma} - S_{4bm}(k)i_{mb} - S_{4cm}(k)i_{mc} \tag{6}$$

where i_B is the BESS current, S_{1xm} and S_{4xm} are the upper and lower switches of each inverter phase, and i_{mx} are the phase currents. Due to the redundancies of the voltage vectors, the dynamic equations are written in abc coordinates. The capacitor voltages are predicted as

$$\begin{bmatrix} v_{dc1m}(k+1) \\ v_{dc2m}(k+1) \end{bmatrix} = \begin{bmatrix} v_{dc1m}(k) \\ v_{dc2m}(k) \end{bmatrix} + \frac{T_s}{C} \begin{bmatrix} 1 & 0 \\ 0 & 1 \end{bmatrix} \begin{bmatrix} i_{mdc1}(k) \\ i_{mdc2}(k) \end{bmatrix} \tag{7}$$

or

$$\mathbf{v}_{dcm}(k+1) = \mathbf{v}_{dcm}(k) + \mathbf{D}_m \mathbf{i}_{mdc}(k) \tag{8}$$

where C is the capacitance of the dc bus capacitors.

Considering all the control objectives of the master NPC, its cost function can be designed as

$$\begin{aligned} g_m = {} & \lambda_1(\mathbf{v}^*_{m\alpha\beta}(k+2) - \mathbf{v}_{m\alpha\beta}(k+2))^2 \\ & + \lambda_2(\mathbf{i}^*_{m\alpha\beta}(k+1) - \mathbf{i}_{m\alpha\beta}(k+1))^2 \\ & + \lambda_3(\mathbf{v}_{dcm}(k+1) - \mathbf{v}^*_{dcm}(k+1))^2 + I_{lim} \end{aligned} \tag{9}$$

where λ_1, λ_2, and λ_3 are weighting factors, $\mathbf{v}^*_{m\alpha\beta}(k+2)$ and $\mathbf{v}^*_{dc}(k+1)$ are the voltage references for the *LC* filter and dc bus and $\mathbf{i}^*_{m\alpha\beta}(k+1)$ are the current references. The term I_{lim} limits the amplitude of the inverter-side currents: if the absolute value of $\mathbf{i}_{m\alpha\beta}(k+1))$ is larger than the inverter maximum current, I_{lim} assumes a large value and zero otherwise [21], [22]. At each k, (9) is evaluated for all 27 inverter voltage vectors, and the one that minimizes it is implemented. The voltage and current references depend on the microgrid mode and will be described in Section III.

B. Slave Inverters

The slaves are two equal grid-following NPC inverters with PV panels and *LCL* filters. They control the inverter-side currents to control the power, and balance the dc bus capacitors voltages. The grid-side currents could be controlled instead of the inverter-side ones, but this is a more complex problem. The voltages of the *LCL* filter capacitors could also be included in the cost function [20], [22], [37], but, as the aim here is to provide load currents, this is not necessary; instead, they are considered disturbances, yielding a simplified first-order model [15], [17]. The discrete-time inverter-side currents in $\alpha\beta$ are

$$\begin{aligned} \begin{bmatrix} i_{s\alpha}(k+1) \\ i_{s\beta}(k+1) \end{bmatrix} = {} & \left(1 - \frac{RT_s}{L_s}\right) \begin{bmatrix} 1 & 0 \\ 0 & 1 \end{bmatrix} \begin{bmatrix} i_{s\alpha}(k) \\ i_{s\beta}(k) \end{bmatrix} \\ & + \frac{T_s}{L_s} \begin{bmatrix} 1 & 0 \\ 0 & 1 \end{bmatrix} \begin{bmatrix} u_{s\alpha}(k) \\ u_{s\beta}(k) \end{bmatrix} - \frac{T_s}{L_s} \begin{bmatrix} 1 & 0 \\ 0 & 1 \end{bmatrix} \begin{bmatrix} v_{s\alpha}(k) \\ v_{s\beta}(k) \end{bmatrix} \end{aligned} \tag{10}$$

or, in compact form

$$\mathbf{i}_{s\alpha\beta}(k+1) = \mathbf{A}_{si}\mathbf{i}_{s\alpha\beta}(k) + \mathbf{B}_{si}\mathbf{u}_{s\alpha\beta}(k) - \mathbf{F}_{si}\mathbf{v}_{s\alpha\beta}(k) \tag{11}$$

where $\mathbf{i}_{s\alpha\beta}$ are the inverter-side currents, $\mathbf{u}_{s\alpha\beta}$ are the inverter output voltages, $\mathbf{v}_{s\alpha\beta}$ are the filter capacitor voltages, and L_s, C_s, and R are the filter parameters. This model was also discretized by Euler.

For the control of the dc bus voltage, the currents that flow through the upper and lower capacitors i_{sdc1} and i_{sdc2} are

$$i_{sdc1} = i_{\mathrm{PV}} - S_{1as}(k)i_{sa} - S_{1bs}(k)i_{sb} - S_{1cs}(k)i_{sc} \tag{12}$$

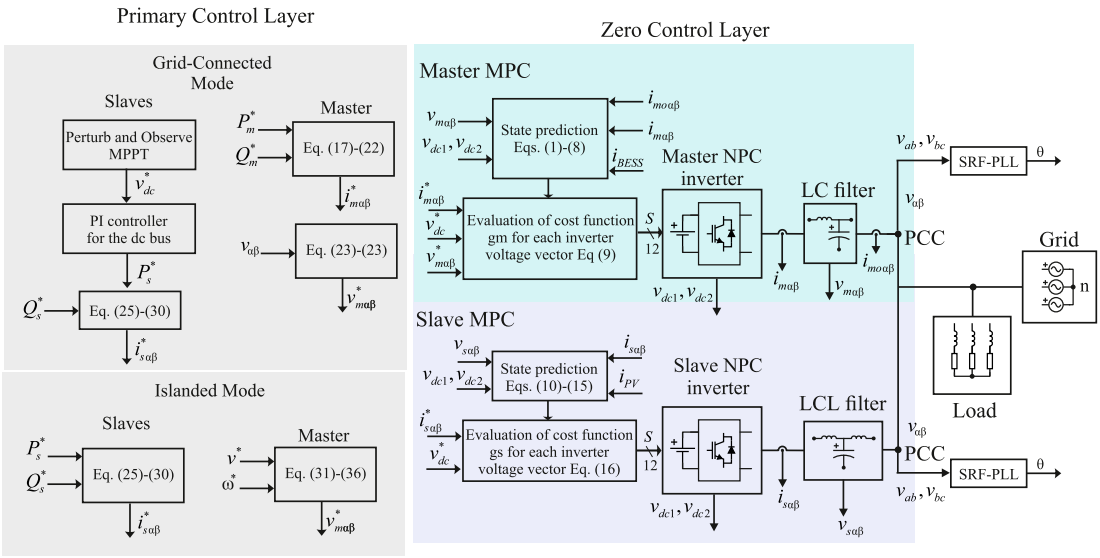

Fig. 2. Block diagram of the proposed master-slave FCS-MPC.

$$i_{sdc2} = i_{PV} + S_{4as}(k)i_{sa} - S_{4bs}(k)i_{sb} - S_{4cs}(k)i_{sc} \quad (13)$$

where i_{PV} is the current from the PV panels, S_{1xs} and S_{4xs} are the upper and lower switches of each inverter phase, and i_{sx} are the phase currents. Again, the equations are written in abc coordinates due to the redundancies of the voltage vectors, and the capacitor voltages are

$$\begin{bmatrix} v_{dc1s}(k+1) \\ v_{dc2s}(k+1) \end{bmatrix} = \begin{bmatrix} v_{dc1s}(k) \\ v_{dc2s}(k) \end{bmatrix} + \frac{T_s}{C} \begin{bmatrix} 1 & 0 \\ 0 & 1 \end{bmatrix} \begin{bmatrix} i_{sdc1}(k) \\ i_{sdc2}(k) \end{bmatrix} \quad (14)$$

or

$$\mathbf{v}_{dcs}(k+1) = \mathbf{v}_{dcs}(k) + \mathbf{D}_s \mathbf{i}_{sdc}(k) \quad (15)$$

where C is the capacitance of the dc bus capacitors.

Considering all the control objectives of the Slave NPCs, their cost functions can be written as

$$g_s = \lambda_1(\mathbf{i}^*_{s\alpha\beta}(k+1) - \mathbf{i}_{s\alpha\beta}(k+1))^2 + \lambda_2(\mathbf{v}_{dcs}(k+1) - \mathbf{v}^*_{dcs}(k+1))^2 + I_{lim} \quad (16)$$

where λ_1 and λ_2 are weighting factors, and $\mathbf{i}^*_{s\alpha\beta}(k+1)$ and $\mathbf{v}^*_{dcs}(k+1)$ are the current and dc bus voltage references. At each k, (16) is calculated for all 27 inverter voltage vectors and the one that minimizes it is implemented. The current references will be described in Section III. The block diagram of the proposed master-slave FCS-MPC is shown in Fig. 2.

The proposed master-slave uses FCS-MPC for the inner current and voltage loops. Therefore, the voltage vector to be applied over T_s is chosen by solving a standard optimization problem, where the cost function is calculated for all inverter voltage vectors. The authors in [21] and [22] considered two-level inverters, so the optimization problem loop needs to be solved eight times. In this article, it needs to be solved 27 times for all NPC voltage vectors, resulting in a higher computational burden. However, the FCS-MPC formulation is simple and straightforward. The authors in [15] and [17] presented modulated MPCs with faster execution time and lower computational burden than the FCS-MPC used in this article, at the expense of a more complex problem formulation and algorithm implementation.

C. Extra Control Loops

For the slaves, a "perturb and observe" maximum power point tracking (MPPT) was implemented to provide the total dc bus voltage reference. A synchronous reference frame phase locked loop (SRF-PLL) was used to synchronize the master and slaves to the grid in grid-connected mode, and the slaves to the grid-forming master when islanded [38]. A positive sequence detector (PSD) was added to the SRF-PLL to improve its performance for weak grids [38].

III. Microgrid Primary Control

In this article, two operational modes are proposed for the microgrid primary control. In the first, the microgrid is connected to the grid, and the master and slaves are grid-following inverters. In the second, the microgrid is islanded, and the master operates as a grid-forming inverter. To control the inverters in both modes, the current and voltage references for the inner FCS-MPCs presented in Section II must be properly defined, as will be described in the following.

A. Grid-Connected Mode

In this mode, the microgrid is connected to the grid. The master is a grid-following inverter, synchronized to the grid by the SRF-PLL. An open-loop PQ control is used [38] to calculate the grid-side current references for the master

$$i^*_{mo\alpha}(k) = \frac{2}{3} \frac{1}{v^2_{m\alpha}(k) + v^2_{m\beta}(k)} (v_{m\alpha}(k)P^*_m + v_{m\beta}(k)Q^*_m) \quad (17)$$

$$i^*_{mo\beta}(k) = \frac{2}{3}\frac{1}{v^2_{m\alpha}(k) + v^2_{m\beta}(k)}(v_{m\beta}(k)P^*_m - v_{m\alpha}Q^*_m(k)) \tag{18}$$

where P^*_m and Q^*_m are the master active and reactive power references, that come from the secondary control layer (out of the scope of this article). To obtain the inverter-side current references, the reactive power of the *LC* filter is compensated

$$i^*_{\alpha m}(k) = i^*_{mo\alpha}(k) - 2\pi f C_m v_{m\beta}(k) \tag{19}$$

$$i^*_{\beta m}(k) = i^*_{mo\beta}(k) + 2\pi f C_m v_{m\alpha}(k) \tag{20}$$

where f is grid frequency that comes from the SRF-PLL. Then, the references are extrapolated to $(k+1)$

$$i^*_{m\alpha}(k+1) = i^*_{m\alpha}(k)\cos(\omega T_s) - i^*_{m\beta}(k)\sin(\omega T_s) \tag{21}$$

$$i^*_{m\beta}(k+1) = i^*_{m\beta}(k)\cos(\omega T_s) + i^*_{m\alpha}(k)\sin(\omega T_s). \tag{22}$$

The voltage references for the master can be defined as the voltages measured at the point of common coupling (PCC) shown in Fig. 2, and are extrapolated to $(k+2)$ as

$$v^*_{m\alpha}(k+2) = v^*_{\alpha}(k)\cos(2\omega T_s) - v^*_{\beta}(k)\sin(2\omega T_s) \tag{23}$$

$$v^*_{m\beta}(k+2) = v^*_{\beta}(k)\cos(2\omega T_s) + v^*_{\alpha}(k)\sin(2\omega T_s). \tag{24}$$

For the grid-following slaves, the current references are

$$i^*_{so\alpha}(k) = \frac{2}{3}\frac{1}{v^2_{s\alpha}(k) + v^2_{s\beta}(k)}(v_{s\alpha}(k)P^*_s + v_{s\beta}(k)Q^*_s) \tag{25}$$

$$i^*_{so\beta}(k) = \frac{2}{3}\frac{1}{v^2_{s\alpha}(k) + v^2_{s\beta}(k)}(v_{s\beta}(k)P^*_s - v_{s\alpha}Q^*_s(k)) \tag{26}$$

P^*_s and Q^*_s come from the MPPT and the dc bus voltage control loop that can be implemented by a PI controller. As for the master, $i^*_{so\alpha}(k)$ and $i^*_{so\beta}(k)$ are the grid-side references. The inverter-side current references are obtained by compensating the reactive power of the *LCL* filter capacitors

$$i^*_{s\alpha}(k) = i^*_{o\alpha}(k) - 2\pi f C_s v_{s\beta}(k) \tag{27}$$

$$i^*_{s\beta}(k) = i^*_{o\beta}(k) + 2\pi f C_s v_{s\alpha}(k). \tag{28}$$

Then, the references are extrapolated to (k+1)

$$i^*_{s\alpha}(k+1) = i^*_{s\alpha}(k)\cos(\omega T_s) - i^*_{s\beta}(k)\sin(\omega T_s) \tag{29}$$

$$i^*_{s\beta}(k+1) = i^*_{s\beta}(k)\cos(\omega T_s) + i^*_{s\alpha}(k)\sin(\omega T_s) \tag{30}$$

B. Islanded Mode

When islanded, the master is a grid-forming inverter. It also provides one-third of the load power, performing power sharing with the slaves, and the three inverters provide the total load apparent power. For grid-forming operation, an outer droop control was implemented for the master [21], [22]

$$v^*(k) = v_{\text{nom}} - k_p(P^*_m - P_m(k)) \tag{31}$$

$$\omega^*(k) = \omega_{\text{nom}} + k_q(Q^*_m - Q_m(k)) \tag{32}$$

where v^* is the amplitude voltage reference, v_{nom} is the microgrid nominal voltage, ω^* is the reference frequency, ω_{nom} is the microgrid nominal frequency, k_p and k_q are the droop coefficients,

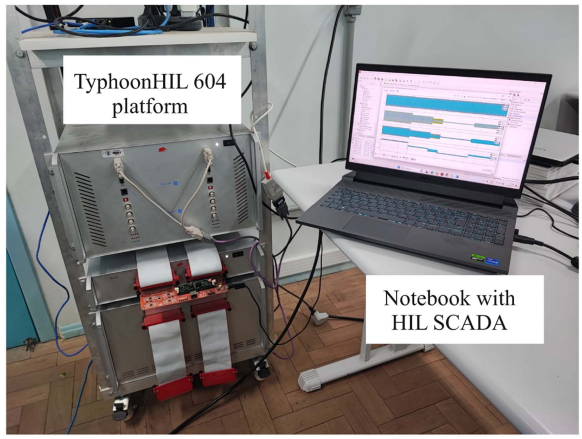

Fig. 3. Typhoon HIL 604 HIL platform.

and P_m and Q_m are the instantaneous active and reactive powers of the master, calculated as

$$P_m(k) = v_{m\alpha}(k)i_{m\alpha}(k) + v_{m\beta}(k)i_{m\beta}(k) \tag{33}$$

$$Q_m(k) = v_{m\beta}(k)i_{m\alpha}(k) - v_{m\alpha}(k)i_{m\beta}(k). \tag{34}$$

The voltage references for the master are

$$v^*_{m\alpha}(k) = v^*(k)\cos(\omega T_s) \tag{35}$$

$$v^*_{m\beta}(k) = v^*(k)\sin(\omega T_s) \tag{36}$$

which are extrapolated to $(k+2)$ as in (23) and (24). For islanded mode, the current term in the cost function (9) is removed.

The slaves also operate as grid-following inverters but are now synchronized to the master. However, they do not operate with MPPT, but instead as semidispatchable generating units. They are controlled so that P^*_s and Q^*_s for each slave are set as one-third of the load active and reactive powers, and the three inverters perform power sharing to feed the total load apparent power. Due to environmental conditions like partial shading, at night or on rainy days, the slaves may not be able to properly supply the load. In these cases, the master delivers more than one-third of the load power to compensate for the lack of PV generation, or even provides the total load power. These particular conditions will be described in the case studies presented in the next section.

IV. Case Studies

To validate the proposed master–slave FCS-MPC, the microgrid of Fig. 1 was implemented in a Typhoon HIL 604 HIL platform, shown in Fig. 3. The system parameters are presented in Table I. The BESS is composed of lithium-ion batteries with a nominal voltage of 800 V and 500 Ah capacity.The controllers were implemented in the ARM core of Typhoon HIL 604, which includes the processor implementation delay. As a result, in (9), the currents are predicted for $k+2$ and the voltages for $k+3$, while in (16), the currents are predicted for $k+2$. The disturbances (grid voltages, master grid-side currents, and slave capacitor voltages) are also estimated for $k+2$. The weighting factors were obtained heuristically, resulting in $\lambda_1 = 1000, \lambda_2 = 300$, and $\lambda_3 = 100$ for the master, and $\lambda_1 = 800$ and $\lambda_2 = 100$

TABLE I
SYSTEM PARAMETERS FOR THE CASE STUDIES

Parameter	Value
Total dc-link voltage	800 V
Rated power (Master)	100 kVA
Rated power (Slaves)	50 kVA
LCL filter (Slaves)	3.3 mH; 300 μF; 200 μH
LC filter (Master)	3 mH; 500 μF
R (Master and Slaves)	0.012 Ω
Filter damping resistor (Master)	0.5 Ω
Filter damping resistor (Slaves)	2 Ω
Line impedance	Z_l = 20μH, 0.01Ω
Grid impedance (strong grid)	Z_g = 2.7μH, 0.01Ω
Grid SCR (strong grid)	72.34
Grid impedance (weak grid)	Z_g = 100μH, 0.3Ω
Grid SCR (weak grid)	2.41
Grid voltage	220Vrms; 50Hz
Sampling frequency f_s	20kHz
Dead time	0.5e-6s

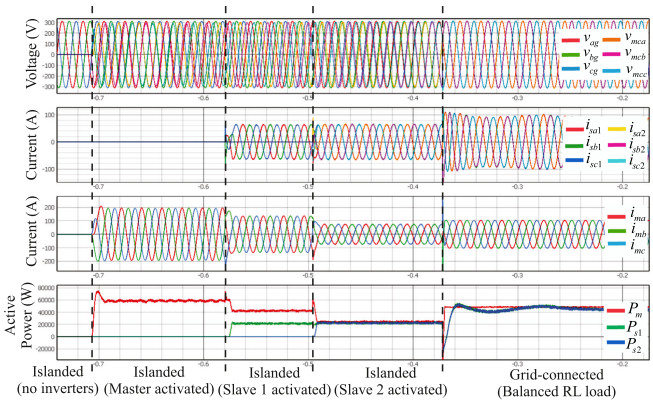

Fig. 4. Case study A: Master capacitor voltages and grid voltages; grid-side currents of Master and Slaves; active powers of Master and Slaves.

for the slaves. A strong grid is considered, with an impedance of $R = 0.01\ \Omega$ and $L = 2.7\ \mu$H and a three-phase power of 14.47 MVA. As seen from Table I, the total inverter power is equal to 200 kVA. The short-circuit ratio (SCR), calculated here as the ratio of the grid power to the sum of the inverter powers, is 72.34. In the following, case studies for different operational conditions will be provided to demonstrate the good performance of the proposed master-slave FCS-MPC.

A. Black-Start, Power Sharing, and Synchronization

The microgrid black-start and its connection and synchronization to the grid are presented in Fig. 4 that shows, from top to bottom, the master capacitor voltages and the grid voltages, the grid-side currents of both slaves, the master grid-side currents and the master and slaves active powers. First, the microgrid is islanded with a balanced RL load ($R = 1.03\ \Omega$ and $L = 3.3$ mH). The master is activated first, operating as a grid-forming inverter and providing full-load power. Then, Slave 1 is activated, and it is controlled to provide one-third of the total load power, while the master provides the remaining power. Finally, Slave 2 is activated, and the total load power is equally shared by all

TABLE II
THD OF THE GRID-SIDE CURRENTS FOR GRID-TIED MODE

	Master	Slave 1	Slave 2
i_a	1.53%	1.42%	1.42%
i_b	1.39%	1.24%	1.24%
i_c	1.48%	1.28%	1.28%

TABLE III
THD OF THE FILTER VOLTAGES FOR ISLANDED MODE

	Master	Slave 1	Slave 2
v_a	1.46%	1.56%	1.56%
v_b	1.24%	1.51%	1.51%
v_c	1.21%	1.49%	1.49%

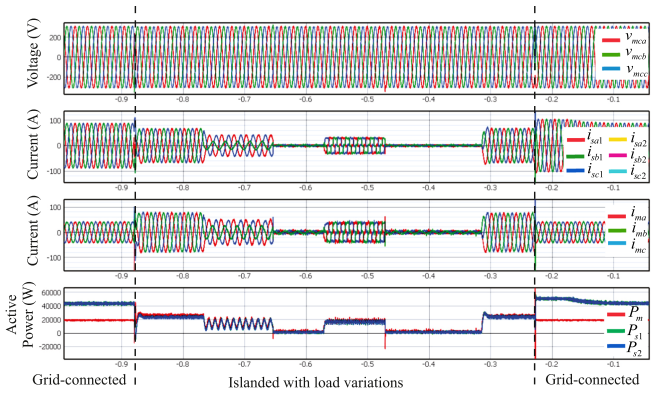

Fig. 5. Case study B1: Master capacitor voltages; grid-side currents of Master and Slaves; active powers of Master and Slaves.

inverters. When the microgrid is connected to the grid by closing switch S_1, the inverters quickly synchronize to the grid, as can be seen by the master voltages. The overcurrents in the connection transient are measured on the grid side; the inverter-side currents are limited by the cost functions. In grid-connected mode, the master seamlessly changes to voltage and current control, injecting 50 kW into the grid in this example, and the Slaves operate with MPPT. The transient from islanded to grid-tied is slower for the slaves due to the dynamics of the MPPT and of the outer PI for the dc bus voltage control.

The total harmonic distortion (THD) of the grid-side currents for the slaves and master for grid-connected mode are shown in Table II. The peak current of the slaves with MPPT is 87 A. The master injects 50 kW into the grid, resulting in peak currents of 102 A. The current THD may change depending on the amplitude of the grid-side currents. The THD of the filter capacitor voltages for the slaves and master in islanded mode are shown in Table III, considering the balanced RL load. For other loads, the voltage THD may change.

B. Transition From Grid-Connected to Islanded, Load Changes, and Transition From Islanded to Grid-Connected

In this case, the microgrid transitions from grid-connected to islanded mode and vice versa, and dynamic load changes are applied when islanded. The results are shown in Fig. 5, which presents the same waveforms as Fig. 4. When the microgrid is

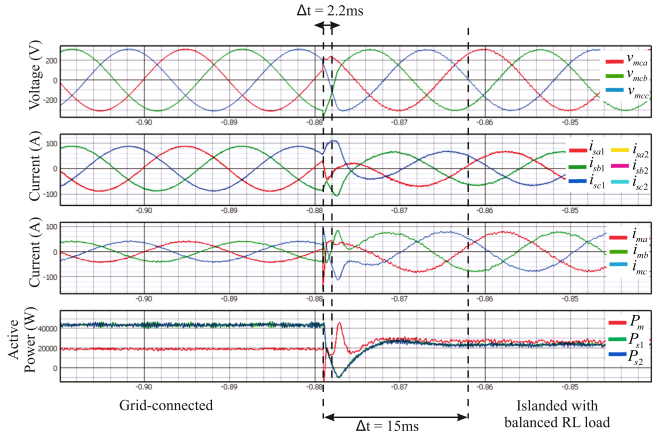

Fig. 6. Case study B1: Zoom in the Master capacitor voltages; grid-side currents of Master and Slaves; active powers of Master and Slaves.

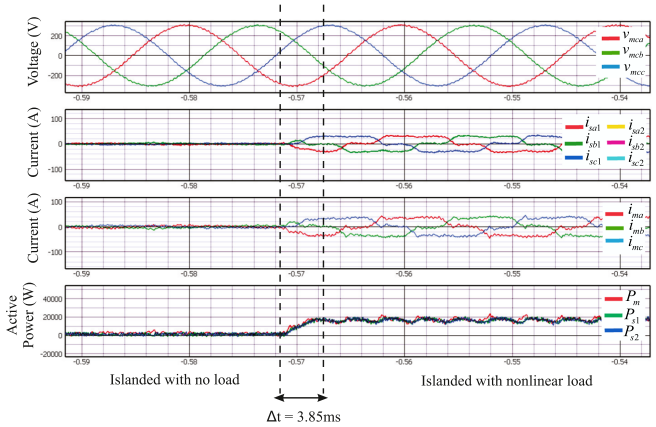

Fig. 7. Case study B1: Zoom in the Master capacitor voltages; grid-side currents of Master and slaves; active powers of Master and slaves.

grid-connected, the Slaves operate with MPPT, and the Master injects 20 kW into the grid with the same balanced RL load. Then, the microgrid is islanded, and the Slaves operate as semidispatchable units, each providing one-third of the total load power. The Master provides the difference between the total load power and the power delivered by the Slaves. After the microgrid is islanded, the load is changed to: 1) unbalanced RL load ($R_a = 1.03\ \Omega$ and $L_a = 3.3$ mH, $R_b = 6\ \Omega$ and $L_b = 12$ mH and $R_c = 2\ \Omega$ and $L_c = 6$ mH); 2) no load; 3) nonlinear load (three-phase diode rectifier with inductive input filter with $L = 1$ mH and output RL load with $R = \Omega$ and $L = 5$ mH); 4) no load; 5) balanced RL load. The Slaves and the Master respond very fast to these load changes, properly performing power sharing. Finally, the microgrid is again connected to the grid, and results similar to Fig. 4 are seen. To illustrate some of the transient responses, Figs. 6 and 7 show a zoom in the waveforms of Fig. 5 for the transition from grid-connected to islanded mode with balanced RL load and from islanded with no load to nonlinear load. The measured approximate responses for the events shown in Fig. 5 are as follows.

1) Grid-tied to islanded: 15 ms (Master and Slave currents and active power) and 2.2 ms (Master voltages).

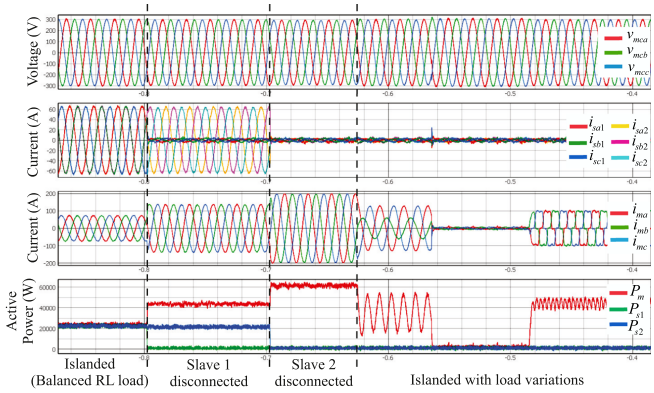

Fig. 8. Case study B2: Master capacitor voltages; grid-side currents of Master and slaves; active powers of Master and slaves.

2) First load change: 0.81 ms (Master and Slave currents and active power). The transient response of the Master voltages is almost imperceptible.
3) Second load change: 0.35 ms (Master and Slave currents and active power). The transient response of the Master voltages is almost imperceptible.
4) Third load change: 3.85 ms (Master and Slave currents and active power). The transient response of the Master voltages is almost imperceptible.
5) Fourth load change: 1.07 ms (Master and Slave currents and active power) and 0.43 ms (Master voltages)
6) Fifth load change: 10.2 ms (Master and Slave currents and active power). The transient response of the Master voltages is almost imperceptible.
7) Islanded to grid-tied: 127.74 ms (Slave currents and active power) and 2.39 ms (Master currents and power). The transient response of the Master voltages is almost imperceptible. The slower response of the Slaves happens because, when they reconnect to the grid, they change to MPPT with PI for dc bus voltage control, and these two outer control loops have slow transient responses.

Another power-sharing scenario is analyzed when the microgrid is islanded, and the results are shown in Fig. 8. First, the balanced RL load is connected to the microgrid and all inverters are active. Then, Slave 1 is turned off (for example, if there is not enough irradiation), and the Master takes over the power that should be delivered by Slave 1. Finally, Slave 2 is also turned off, and the Master provides the full load power. With only the Master active, the same load variations of Fig. 5 are performed. These results show that the Master is able to properly provide the total load power, compensating the absence of the Slaves, while acting as a grid-forming inverter. As seen in Section II, the load is not included in the mathematical model of the system, and consequently, these results demonstrate the good performance of the proposed Master-Slave FCS-MPC with respect to unmodeled dynamics.

In this article, it is assumed that the state-of-charge (SOC) of the BESS is enough for the case studies, and SOC management is not considered. However, there are several ways to address this; for example, the BESS could be recharged when there is more PV power than load demand in islanded mode, or by the

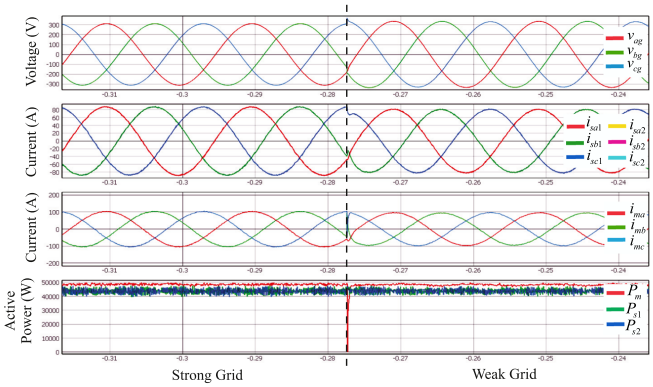

Fig. 9. Case study C: Grid voltages; grid-side currents of Master and slaves; active powers of Master and slaves.

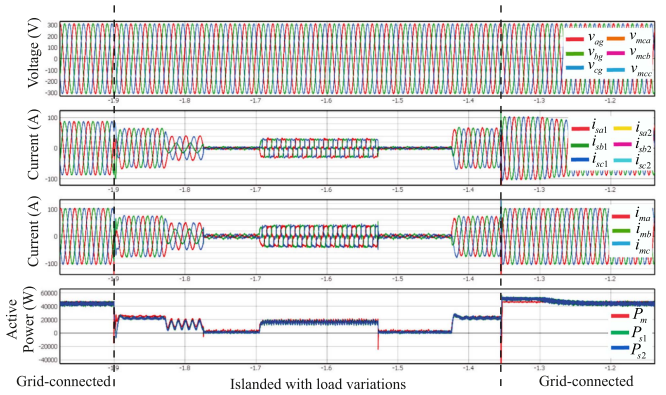

Fig. 10. Case study D1: Master capacitor voltages; grid-side currents of Master and slaves; active powers of Master and slaves.

grid in grid-connected mode. In the first case, the control of the slaves could include an operational mode to recharge the Master. This would be done by the inclusion of SOC and power management in the secondary and tertiary control layers of the microgrid, which are out of the scope of the present article but will be included in future works.

C. Operation With Weak Grid

It is also important to verify the performance of the proposed Master-Slave FCS-MPC with weak grids. To do so, a weak grid with impedance $R = 0.3\ \Omega$ and $L = 100\ \mu$H is considered, with three-phase power of 481 kVA and SCR $= 2.41$ (a grid with SCR lower than 5 is considered weak). The results are seen in Fig. 9, which shows in the right-side the strong grid waveforms. The slaves operate with MPPT, the Master injects 50 kW into the grid, and the balanced RL load is connected. Then, the grid impedance is changed, as shown in the left side of Fig. 9. For a weak grid, a slight overvoltage is observed in the grid voltages; this can be mitigated by including extra power curtailment and/or reactive power compensation functionalities in the inverter control. However, the Master and slaves operate properly, providing adequate currents for both strong and weak grids. The grid impedance is not included in the mathematical model of the system, and these results demonstrate the good performance of the proposed Master-Slave FCS-MPC with unmodeled dynamics.

D. Parameter Mismatches in the LC Filter of the Master

To verify the robustness of the Master to parameter mismatches, the *LC* filter parameters are increased and decreased by 50% in the system but are equal to the nominal values in the model equations. These results are seen in Figs. 10 and 11, which show the same waveforms, transients, and load changes as Fig. 5, but the Master is controlled to inject 50 kW when grid-connected. Fig. 10 shows the results for a 50% increase in the filter parameters; the nominal values are presented in Table I, and the increased ones are $R = 0.018\ \Omega$, $L = 4.5$ mH, and $C = 750\ \mu$F. The Master and the slaves (with nominal filter values) operate properly for all load variations and transients.

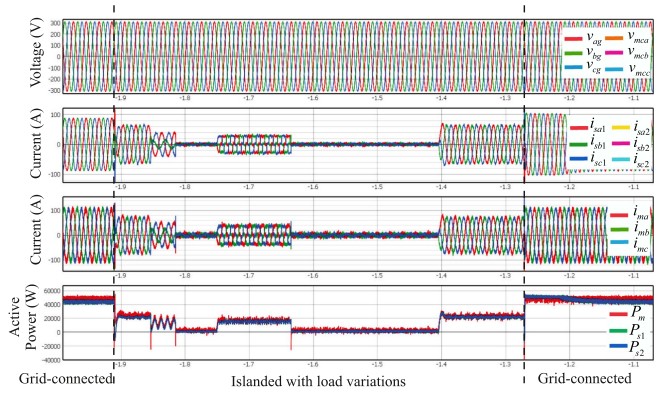

Fig. 11. Case study D2: Master capacitor voltages; grid-side currents of Master and slaves; active powers of Master and slaves.

The transient response of the Master is more oscillatory, but otherwise it continues to have a good performance. Fig. 11 shows the same results, but now with the filter parameters of the Master decreased by 50%, to $R = 0.006\ \Omega$, $L = 1.5$ mH, and $C = 350\ \mu$F. The Master operates properly for all operational conditions and transients. There are higher ripples on the output currents, as the filter inductance is smaller than the nominal value. These results demonstrate that the Master presents robustness to parameter mismatches and that the microgrid operates properly and remains stable.

E. Parameter Mismatches in the LCL Filters of the Slaves

Two examples are shown for parameter mismatches in the *LCL* filters of both Slaves, where the filter parameters are increased and decreased by 50% in the system but remain equal to the nominal values in the model. These results are seen in Figs. 12 and 13, with the same conditions as Fig. 5. Fig. 12 shows the results for a 50% increase in the filter parameters, with $R = 0.018\ \Omega$, $L = 4.95$ mH, and $C = 450\ \mu$F. The slaves and the Master (with nominal values) operate properly for all conditions. There is a larger steady-state error in the currents and powers of the Slaves, but the inverters still have fast transient responses and do not become unstable. The load power that is

TABLE IV
COMPARATIVE ANALYSIS

Strategy	Islanded	Grid-connected	Design	Transient response	Power sharing
Proposed Master-Slave FCS-MPC	Yes	Yes	Medium	Fast	Yes
FCS-MPC of [21], [22]	Yes	No	Medium	Fast	Yes
FCS-MPC of [23]	Yes	No	Low	Fast	No
SVM^{2}PC of [17]	Yes	No	Medium	Fast	No
Master-Slave of [6]	Yes	Yes	High	Medium	Yes
Master-Slave of [7]	Yes	No	High	Medium	Yes
Master-Slave of [10]	Yes	No	High	Medium	Yes
Master-Slave of [9]	No	Yes	High	Medium	Yes

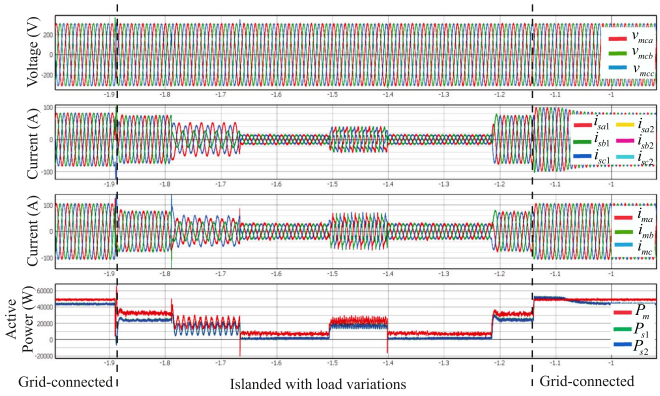

Fig. 12. Case study E1: Master capacitor voltages; grid-side currents of master and slaves; active powers of master and slaves.

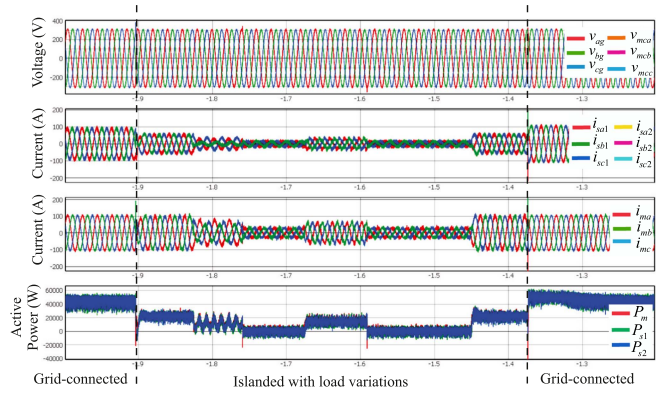

Fig. 13. Case study E2: Master capacitor voltages; grid-side currents of master and slaves; active powers of master and slaves.

not processed by the Slaves due to the high parameter mismatch is compensated by the Master; therefore, the overall microgrid performance is maintained. Fig. 13 shows the same transient results, but for a 50% decrease in the filter parameters, i.e, $R = 0.006\ \Omega$, $L = 1.65$ mH, and $C = 150\ \mu$F. As the filter values are smaller, a larger ripple is observed on the currents and active powers of both Slaves. However, the inverters remain operating with fast transient responses and are stable. Therefore, from these results, it can be stated that the proposed Master-Slave FCS-MPC is stable for the system considered in this study, as it is difficult to prove the stability of systems with MPC in a closed form [13].

V. COMPARATIVE ANALYSIS

In this section, a comparative analysis of the proposed Master-Slave FCS-MPC and other strategies will be presented. The overall comparison is shown in Table IV. The authors in [17], [21], [22], and [23], proposed FCS-MPC strategies for grid-forming inverters, while [6], [7], [9], [10] proposed Master-Slave strategies. As mentioned, up to date, there has been no research incorporating Master-Slave primary control together with the zero layer FCS-MPC for improved microgrid performance.

The fast transient response of the proposed Master-Slave FCS-MPC is comparable to the dynamic performance of the FCS-MPCs of [21], [22], and [23]; however, these papers only address islanded operation. Also, Young et al.[23] do not address power sharing. The design process complexity of the proposed Master-Slave FCS-MPC and [21], [22] is medium, as they need to design the weighting factors for the cost functions, while [23] does not need to design weighting factors. The computation burden of the proposed Master-Slave FCS-MPC is higher than that of [21], [22], and [23], as they used two-level inverters. Therefore, the cost function calculation loop in [21], [22], and [23] is performed eight times for the eight inverter voltage vectors, while in this article, it is calculated 27 times for each NPC inverter. The grid-forming SVM^2 PC of [17] has a very low computational burden but a more complex design procedure; however, it operates with fixed switching frequency.

Regarding Master-Slave strategies, [6] can work on islanded and grid-connected modes with power sharing; however, the robust control with nested linear quadratic regulators and mixed H_2/H_∞ optimal control has a more complex design procedure than the proposed Master-Slave FCS-MPC. Also, as [6] is based on classical controllers, its dynamic response is slower. A similar analysis is valid for the Master-Slave linear controller with cooperative load sharing of [7], the Master-Slave with data-driven three-layer neural network (NN) of [10], and the Master-Slave with SFNNs of [9]. Therefore, based on this discussion, the results of Section IV, and the comparisons of Table IV, it can be stated that the proposed Master-Slave FCS-MPC is a very good alternative for controlling inverters in grid-connected and islanded microgrids.

VI. CONCLUSION

This article proposed a Master-Slave FCS-MPC for the zero and primary control layers of microgrids. Two modes of operation were proposed for the primary control. In grid-connected mode, the Master and Slaves are grid-following inverters. In

islanded mode, the Master is a grid-forming inverter, and the Slaves remain as grid-following. To validate the performance of the proposed Master-Slave FCS-MPC, case studies were presented for grid-connected and islanded modes, with load and parametric variations. The results demonstrate the good performance of the proposed Master-Slave FCS-MPC, such as fast dynamic response, multivariable control, load sharing and robustness to parametric uncertainties/variations in the system and to unmodeled dynamics. It is important to point out that this article is the first step for the implementation of the Master-Slave FCS-MPC with secondary and tertiary control in future works. Also, further improvements can be included in the MPC formulation. Horizon adjustment and simplified cost function design can be used for computational burden reduction, and virtual vector techniques or fixed switching frequency MPC can be used for restricted voltage vector flexibility, therefore improving the performance of the microgrid.

REFERENCES

[1] Z. Zhang et al., "Advances and opportunities in the model predictive control of microgrids: Part I–primary layer," *Int. J. Elect. Power Energy Syst.*, vol. 134, 2022, Art. no. 107411.

[2] J. Hu, Y. Shan, J. M. Guerrero, A. Ioinovici, K. W. Chan, and J. Rodriguez, "Model predictive control of microgrids–An overview," *Renewable Sustain. Energy Rev.*, vol. 136, 2021, Art. no. 110422.

[3] O. Babayomi et al., "Advances and opportunities in the model predictive control of microgrids: Part II–secondary and tertiary layers," *Int. J. Elect. Power Energy Syst.*, vol. 134, 2022, Art. no. 107339.

[4] J. Hu, Y. Shan, K. W. Cheng, and S. Islam, "Overview of power converter control in microgrids-Challenges, advances, and future trends," *IEEE Trans. Power Electron.*, vol. 37, no. 8, pp. 9907–9922, Aug. 2022.

[5] O. Babayomi, Y. Li, Z. Zhang, R. Kennel, and J. Kang, "Overview of model predictive control of converters for islanded AC microgrids," in *Proc. IEEE 9th Int. Power Electron. Motion Control Conf.*, 2020, pp. 1023–1028.

[6] P. Buduma, M. K. Das, R. T. Naayagi, S. Mishra, and G. Panda, "Seamless operation of master-slave organized AC microgrid with robust control, islanding detection, and grid synchronization," *IEEE Trans. Ind. Appl.*, vol. 58, no. 5, pp. 6724–6738, Sep./Oct. 2022.

[7] A. Mortezaei, M. G. Simoes, M. Savaghebi, J. M. Guerrero, and A. Al-Durra, "Cooperative control of multi-masterslave islanded microgrid with power quality enhancement based on conservative power theory," *IEEE Trans. Smart Grid*, vol. 9, no. 4, pp. 2964–2975, Jul. 2018.

[8] D. Miller, G. Mirzaeva, C. D. Townsend, and G. C. Goodwin, "Decentralised droopless control of islanded radial AC microgrids without explicit communication," *IEEE Open J. Ind. Appl.*, vol. 3, pp. 104–113, 2022.

[9] Y. Yang and R.-J. Wai, "Self-constructing fuzzy-neural-network-imitating sliding-mode control for parallel-inverter system in grid-connected microgrid," *IEEE Access*, vol. 9, pp. 167389–167411, 2021.

[10] D.-D. Zheng, S. S. Madani, and A. Karimi, "Data-driven distributed online learning control for islanded microgrids," *IEEE Trans. Emerg. Sel. Topics Circuits Syst.*, vol. 12, no. 1, pp. 194–204, Mar. 2022.

[11] J. G. J. Hu and S. Islam, *Model Predictive Control for Microgrids - From Power Electronics Converters to Energy Management*. London, U.K.: IET, 2021.

[12] J. Rodriguez et al., "State of the art of finite control set model predictive control in power electronics," *IEEE Trans. Ind. Inform.*, vol. 9, no. 2, pp. 1003–1016, May 2013.

[13] S. Vazquez, J. Rodriguez, M. Rivera, L. G. Franquelo, and M. Norambuena, "Model predictive control for power converters and drives: Advances and trends," *IEEE Trans. Ind. Electron.*, vol. 64, no. 2, pp. 935–947, Feb. 2017.

[14] P. Karamanakos, E. Liegmann, T. Geyer, and R. Kennel, "Model predictive control of power electronic systems: Methods, results, and challenges," *IEEE Open J. Ind. Appl.*, vol. 1, pp. 95–114, 2020.

[15] C. R. D. Osório et al., "Modulated model predictive control applied to LCL-filtered grid-tied inverters: A convex optimization approach," *IEEE Open J. Ind. Appl.*, vol. 2, pp. 366–377, 2021.

[16] D. Xiao, K. S. Alam, M. Norambuena, M. F. Rahman, and J. Rodriguez, "Modified modulated model predictive control strategy for a grid-connected converter," *IEEE Trans. Ind. Electron.*, vol. 68, no. 1, pp. 575–585, Jan. 2021.

[17] D. Schuetz et al., "Space vector modulated model predictive control for grid-tied converters," *IEEE Trans. Ind. Inform.*, vol. 19, no. 1, pp. 414–425, Jan. 2023.

[18] X. Chen, W. Wu, N. Gao, H. S. H. Chung, M. Liserre, and F. Blaabjerg, "Finite control set model predictive control for LCL-filtered grid-tied inverter with minimum sensors," *IEEE Trans. Ind. Electron.*, vol. 67, no. 12, pp. 9980–9990, Dec. 2020.

[19] M. G. Judewicz, S. A. González, J. R. Fischer, J. F. Martínez, and D. O. Carrica, "Inverter-side current control of grid-connected voltage source inverters with LCL filter based on generalized predictive control," *IEEE Trans. Emerg. Sel. Topics Power Electron.*, vol. 6, no. 4, pp. 1732–1743, Dec. 2018.

[20] T. Dragičević, "Dynamic stabilization of DC microgrids with predictive control of point-of-load converters," *IEEE Trans. Power Electron.*, vol. 33, no. 12, pp. 10872–10884, Dec. 2018.

[21] T. Dragičević, "Model predictive control of power converters for robust and fast operation of AC microgrids," *IEEE Trans. Power Electron.*, vol. 33, no. 7, pp. 6304–6317, Jul. 2018.

[22] C. Zheng, T. Dragičević, and F. Blaabjerg, "Model predictive control-based virtual inertia emulator for an islanded alternating current microgrid," *IEEE Trans. Ind. Electron.*, vol. 68, no. 8, pp. 7167–7177, Aug. 2021.

[23] H. A. Young, V. A. Marin, C. Pesce, and J. Rodriguez, "Simple finite-control-set model predictive control of grid-forming inverters with LCL filters," *IEEE Access*, vol. 8, pp. 81246–81256, 2020.

[24] I. Khan and S. Doolla, "A PI-MPC based dual-loop controller for grid forming inverters," in *Proc. IEEE Int. Conf. Environ. Elect. Eng. IEEE Ind. Commercial Power Syst. Europe*, 2023, pp. 1–6.

[25] C. Cifuentes, H. Young, P. Burgos, and P. Epul, "Model-free predictive control of a grid-forming inverter based on ARX time series with HIL validation," in *Proc. IEEE CHILEAN Conf. Elect., Electron. Eng., Inf. Commun. Technol.*, 2023, pp. 1–6.

[26] C. Zheng, J. Yang, and Z. Gong, "Efficient finite-set model predictive voltage control of islanded-mode grid-forming inverters with current constraints," *IEEE Access*, vol. 10, pp. 95919–95927, 2022.

[27] C. Hu et al., "A novel modulated model-free predictive control for LC-filtered grid-forming inverters with double-difference updating," *IEEE Trans. Ind. Electron.*, vol. 71, no. 9, pp. 10806–10817, Sep. 2024.

[28] A. B. Kunya and M. Argin, "Model predictive load frequency control of multi-area interconnected power system," in *Proc. IEEE Texas Power Energy Conf.*, 2018, pp. 1–6.

[29] A. Venkat, I. Hiskens, J. Rawlings, and S. Wright, "Distributed MPC strategies with application to power system automatic generation control," *IEEE Trans. Control Syst. Technol.*, vol. 16, no. 6, pp. 1192–1206, Nov. 2008.

[30] G. Lou, W. Gu, Y. Xu, M. Cheng, and W. Liu, "Distributed MPC-based secondary voltage control scheme for autonomous droop-controlled microgrids," *IEEE Trans. Sustain. Energy*, vol. 8, no. 2, pp. 792–804, Apr. 2017.

[31] C. Ahumada, R. Cárdenas, D. Sáez, and J. M. Guerrero, "Secondary control strategies for frequency restoration in islanded microgrids with consideration of communication delays," *IEEE Trans. Smart Grid*, vol. 7, no. 3, pp. 1430–1441, May 2016.

[32] J. Sachs and O. Sawodny, "A two-stage model predictive control strategy for economic diesel-PV-battery island microgrid operation in rural areas," *IEEE Trans. Sustain. Energy*, vol. 7, no. 3, pp. 903–913, Jul. 2016.

[33] Y. Shan, J. Hu, and H. Liu, "A holistic power management strategy of microgrids based on model predictive control and particle swarm optimization," *IEEE Trans. Ind. Inform.*, vol. 18, no. 8, pp. 5115–5126, Aug. 2022.

[34] Y. Shan, J. Hu, K. W. Chan, and S. Islam, "A unified model predictive voltage and current control for microgrids with distributed fuzzy cooperative secondary control," *IEEE Trans. Ind. Inform.*, vol. 17, no. 12, pp. 8024–8034, Dec. 2021.

[35] S. Shahzad, M. A. Abbasi, M. A. Chaudhry, and M. M. Hussain, "Model predictive control strategies in microgrids: A concise revisit," *IEEE Access*, vol. 10, pp. 122211–122225, 2022.

[36] F. Carnielutti, M. Aly, M. Norambuena, and J. Rodriguez, "Model predictive control for master-slave inverters in microgrids," in *Proc. IEEE 48th Annu. Conf. Ind. Electron. Soc.*, 2022, pp. 1–6.

[37] N. Panten, N. Hoffmann, and F. W. Fuchs, "Finite control set model predictive current control for grid-connected voltage-source converters with LCL filters: A study based on different state feedbacks," *IEEE Trans. Power Electron.*, vol. 31, no. 7, pp. 5189–5200, Jul. 2016.

[38] R. Teodorescu, M. Liserre, and P. Rodriguez, *Grid Converters for Photovoltaic and Wind Power Systems*. Hoboken, NJ, USA: Wiley-IEEE Press, 2007.

Fernanda Carnielutti (Member, IEEE) received the bachelor's degree in electrical engineering, and the master's and doctor's degrees in electrical engineering from the Federal University of Santa Maria (UFSM), Santa Maria, Brazil, in 2010, 2012, and 2015, respectively.

She was Professor with UFSM - Campus Cachoeira do Sul, from 2016 to 2018. Currently, she is a Professor with the UFSM - Campus Santa Maria, Researcher with the Power Electronics and Control Research Group, GEPOC. Her research interests include modulation of static power converters, multilevel converters power electronics for renewable energies, and model predictive control.

Dr. Carnielutti is a Member of the of the IEEE Power Electronics, Industrial Electronics, and Industry Application Societies.

Mokhtar Aly (Senior Member, IEEE) received the B.Sc. and M.Sc. degrees in electrical engineering from Aswan University, Aswan, Egypt, in 2007 and 2012, respectively, and the Ph.D. degree in electrical engineering from the Department of Electrical Engineering, Faculty of Information Science and Electrical Engineering, Kyushu University, Fukuoka, Japan, in 2017.

In 2008, he joined the Department of Electrical Engineering, Aswan University, as an Assistant Lecturer, where he has been an Assistant Professor with the Faculty of Engineering since 2017. He worked as a Postdoctoral Researcher with the Solar Energy Research Center (SERC-Chile), Universidad Técnica Federico Santa María, Chile, from 2019 to 2021. He has been an Assistant Professor with Universidad San Sebastián, Santiago, Chile, since 2021. His research interests include reliability of power electronics systems in renewable energy applications, multilevel inverters, fault tolerant control, electric vehicles, and light emitting diode (LED) drivers.

Dr. Aly is a Member in IEEE Power Electronics Society (PELS), IEEE Industrial Electronics Society (IES), and IEEE Power and Energy Society (PES).

Margarita Norambuena (Senior Member, IEEE) received the B.S. and M.Sc. degrees in electrical engineering, in 2013, the Ph.D. degree (*summa cum laude*) in electronics engineering from the Universidad Tecnica Federico Santa Maria (UTFSM), Valparaiso, Chile, in 2017, and the Doktoringenieur (Dr.-Ing.) degree (*summa cum laude*) in electrical and electronic engineering from the Technische Universitat Berlin (TUB), Berlin, Germany, in 2018.

She is currently an Assistant Professor with Universidad Tecnica Federico Santa Maria. Her research interests include multilevel converters, model predictive control of power converters and drives, energy storage systems, renewable energy, and electromobility.

Dr. Norambuena is Associate Editor for *IEEE JESTPE*. She was the recipient of the IEEE IES Student Best Paper Award 2019 for her doctoral work.

Jiefeng Hu (Senior Member, IEEE) received the Ph.D. degree in electrical engineering from the University of Technology Sydney, Ultimo, Australia, in 2013.

He was an Assistant Professor with The Hong Kong Polytechnic University, Kowloon, Hong Kong. Subsequently, he joined Federation University Australia as an Associate Professor and a Program Coordinator of Electrical Engineering. He is currently a Stream Leader of the Centre for New Energy Transition Research, Mount Helen, Australia. He participated in the research of minigrids at Commonwealth Scientific and Industrial Research Organization (CSIRO), Newcastle, Australia. His research interests include renewable energy and smart microgrids.

Dr. Hu is an awardee of the highly prestigious Australian Research Council (ARC) Future Fellowships. He is an Associate Editor for *IET Renewable Power Generation*, *IEEE Access*, and IEEE TRANSACTIONS ON ENERGY CONVERSION.

Josep Guerrero (Fellow, IEEE) received the B.Sc. degree in telecom engineering, the M.Sc. degree in electronics engineering, and the Ph.D. degree in power electronics from the Technical University of Catalonia, Barcelona, Spain, in 1997, 2000, and 2003, respectively, and the M.Sc. degree in psychobiology and cognitive neuroscience from the Institute of Neuroscience (INc), Autonomous University of Barcelona, Bellaterra, Spain, in 2022. He is currently working toward the M.Sc. degree in sleep: physiology and medicine with the University of Murcia, Murcia, Spain.

Since 2011, he has been a Full Professor with AAU Energy, Aalborg University, Aalborg, Denmark, where he is responsible for the Microgrid Research Program. From 2019, he became a Villum Investigator by the Villum Fonden, which supports the Center for Research on Microgrids (CROM), Aalborg University, being the founder and Director of the same center. In 2020, he initiated neuroscience studies and research. In 2023, he joined the Technical University of Catalonia as an ICREA Research Professor. His research interests include different microgrid frameworks like energy microgrids, hydrogen and biomass, water micronets, biological systems, seaport microgrids and electrical ships, airport microgrids and more electrical aircrafts, space microgrids, and smart medical systems. In these fields, he has researched distributed and cyber-physical energy systems, cybersecurity for microgrids and smart grids, neuroscience-inspired artificial intelligence for energy systems, machine learning and applications using signal processing, bioinformatics, bioinspired computing, and natural computing, and quantum computing for complex energy networks.

Dr. Guerrero is an Associate Editor for several IEEE Transactions. He has authored or coauthored more than 1000 journal papers in the fields of microgrids and renewable energy systems, which are cited more than 100 000 times. During ten consecutive years, from 2014 to 2023, he was awarded by Clarivate Analytics as Highly Cited Researcher. In 2021, he received the IEEE Bimal Bose Award for Industrial Electronics Applications in Energy Systems, for his pioneering contributions to renewable energy based microgrids. In 2022, he received the IEEE PES Douglas M. Staszesky Distribution Automation Award, for contributions to making the hierarchical control of microgrid systems a practical reality. He was the recipient of the IEEE Modeling and Control Technical Achievement Award in 2023 for his contributions to modeling and control of power electronics-based microgrids.

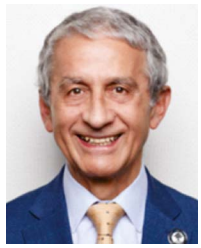

José Rodriguez (Life Fellow, IEEE) received the engineer degree from the Universidad Tecnica Federico Santa Maria, Valparaiso, Chile, in 1977 and the Dr.-Ing. degree from the University of Erlangen, Erlangen, Germany, in 1985, both in electrical engineering.

He has been with the Department of Electronics Engineering, Universidad Tecnica Federico Santa Maria, since 1977, where he was a full Professor and President. From 2015 to 2019, he was the President of Universidad Andres Bello, Santiago, Chile. From 2022 to 2023, he was the President of Universidad San Sebastian, Santiago. He is currently the Director of the Center for Energy Transition, Universidad San Sebastian. He has coauthored two books, several book chapters, and more than 900 journal and conference papers. His main research interests include multilevel inverters, new converter topologies, control of power converters, and adjustable-speed drives.

Dr. Rodriguez has received a number of best paper awards from journals of the IEEE. He is a Member of the Chilean Academy of Engineering. In 2014, he received the National Award of Applied Sciences and Technology from the government of Chile. In 2015, he received the Eugene Mittelmann Award from the Industrial Electronics Society of the IEEE. From 2014 to 2023, he has been included in the list of Highly Cited Researchers published by Web of Science.